AIMS Environmental Science

AIMS Environmental Science, 11(2): 324–341
DOI: 10.3934/environsci.2024015
Received: 12 October 2023
Revised: 26 December 2023
Accepted: 14 May 2024
Published: 23 May 2024

http://www.aimspress.com/journal/environmental

Research article

Enhancing photocatalytic efficiency with Mn-doped ZnO composite carbon nanofibers for organic dye degradation

Krittiya Singcharoen[1], Ratthapol Rangkupan[2,*], Soontree Khuntong[3] and Thanakorn Wasanapiarnpong[4,5,*]

[1] Nanoscience and Technology (International Program), Graduate School, Chulalongkorn University, Bangkok 10330, Thailand
[2] Metallurgy and Materials Science Research Institute, Chulalongkorn University, Bangkok 10330, Thailand
[3] Faculty of Science at Sriracha, Kasetsart University Sriracha Campus, Chonburi 20230, Thailand
[4] Department of Materials of Science, Faculty of Science, Chulalongkorn University, Bangkok 10330, Thailand
[5] Center of Excellence on Petrochemical and Materials Technology, Chulalongkorn University, Bangkok 10330, Thailand

* **Correspondence:** Email: ratthapol.r@chula.ac.th, thanakorn.w@chula.ac.th; Tel: +662181819, +662185541.

Abstract: In this study, Mn-doped ZnO composite carbon nanofibers (Mn-ZnO/CNFs) were prepared via a simple blending and electrospinning (ES) method, followed by a thermal treatment. These fibers were used to investigate the photocatalytic degradation of an organic dye under UV and visible light irradiation. The results showed that Mn-ZnO/CNFs were successfully prepared under the same conditions used for CNFs preparation conditions, which induced a morphological change from a smooth to a rough surface compared to the CNFs. Energy dispersive X-ray (EDX), x-ray diffraction (XRD), and x-ray photoelectron spectroscopy (XPS) analyses confirmed the formation of Mn-doped ZnO on the CNFs' surface. Furthermore, the addition of the catalyst significantly increased in the specific surface area, and a N_2 adsorption-desorption isotherm analysis revealed that all samples had mesoporous characteristics with a type IV isotherm index. The photocatalytic activity of the Mn-ZnO/CNFs carbonized at 650 ℃ using methylene blue (MB) dye as a model pollutant was investigated. All prepared samples effectively removed the MB with a degradation rate of 70-90%. The kinetic reaction rate was described using the simplified Langmuir-Hinshelwood equation. Overall, the CNFs

and composites nanofibers developed through moderate thermal treatment processes possessed a high specific surface area and oxygen vacancy, enabling their potential use as adsorbents and as a catalyst support for reactions at room-to-elevated temperatures, as well as photocatalysts for the removal of organic contaminants.

Keywords: carbon nanofibers; Mn-doped zinc oxide; electrospinning; photocatalysis; organic dye

1. Introduction

The presence of an organic dye in polluted wastewater is a global concern due to their adverse health effects and impact on the quality of human life [1]. Various technologies, such as adsorption, precipitation, filtration, and photocatalysis, have been developed to remove these pollutants [2]. Among them, photocatalysis is particularly promising, noted for being environmentally friendly, sustainable, and cost-effective [3]. It uses semiconductor photocatalysis that absorbs ultraviolet (UV) light energy for generating electron-hole pairs. Then, these pairs react with the organic dye molecules, converting them into harmless molecules such as water (H_2O) and carbon dioxide (CO_2) [4]. This process generates reactive oxygen species (ROS) such as hydroxyl radicals (•OH), which have strong oxidative properties that can break down organic molecules [5]. Photocatalysis can degrade a wide range of organic dyes, including those resistant to conventional treatment methods [6]. As a sustainable technology, it doesn't require additional chemicals or reagents and can be powered by renewable sources such as solar energy [7]. Therefore, photocatalysis holds a great potential as an effective and environmentally friendly solution for removing organic dye pollutants from wastewater.

Zinc oxide (ZnO) is widely used as an extensive photocatalyst, and is renowned for its excellent oxidation capacity, good physical and chemical stability, high photosensitivity, large exciton binding energy (60 meV), non-toxicity, and cost-effectiveness [8,9]. However, ZnO's band gap of 3.37 eV limits its ability to utilize visible light for photocatalysis. Additionally, the rapid recombination of photogenerated electron-hole (e^-- h^+) pairs hinders ZnO's overall photocatalytic activity. Moreover, during the photocatalytic process, the dispersion of ZnO particles in wastewater can lead to pollution and create challenges in their separation after treatment [10,11]. To overcome these limitations, researchers have explored doping ZnO with transition metals, such as manganese (Mn), as a potential solution. Doping ZnO with Mn has been shown to reduce the band gap energy, thus enhancing the absorption of visible light. The presence of Mn introduces additional electronic states, thus promoting a more efficient utilization of visible light [12–14]. Furthermore, the half-filled d^5 electronic configuration of Mn creates abundant electronic states and does not act as a recombination center, which mitigates the rapid recombination of e^-- h^+ pairs. In addition to the electronic band structure, the size and morphology of ZnO also play a pivotal role in determining its photocatalytic activity [15–17]. Nanofibers have gained attention for their potential to increase the surface area of photocatalysts when used in composites or when incorporated with ZnO. They offer an enormous surface area, which minimizes the recombination of charge carriers and provides numerous active sites for photocatalytic reactions [18,19]. Additionally, the flexibility of nanofibers during photocatalytic activities allows for a better accessibility to the dye molecules, as well as reusability and recoverability for subsequent reactions [20]. Recently, carbonaceous materials such as carbon nanofibers (CNFs), primarily produced from polyacrylonitrile (PAN), have been employed in composites and hybrids with ZnO.

They have garnered significant attention due to their ability to enhance visible-light photocatalytic activity, their ease of separation after treatment, and their inherent flexibility. The combination of ZnO and CNFs results in a highly efficient photocatalytic system that improves the degradation of organic dye pollutants while reducing the environmental impact [21]. Thus, using CNFs as a composite material for ZnO represents a promising avenue to develop highly efficient and sustainable photocatalysts for the wastewater treatment [22]. However, reports on Mn-doped ZnO decorated carbon nanofibers for photocatalytic degradation of organic dye pollutants are still limited [23–26].

In this study, we aim to fabricate Mn-doped ZnO composited carbon nanofibers using a simple-step blending and electrospinning method, followed by a thermal treatment. The resulting nanofibers will be utilized to investigate the photocatalytic degradation of organic dye pollutants under irradiation from both UV and visible light. The goal of this study is to explore the potential of Mn-doped ZnO decorated carbon nanofibers as a highly efficient and sustainable photocatalyst for wastewater treatment.

2. Materials and methods

2.1. Materials

PAN with a molecular weight of 150,000 g/mol was procured from Sigma Aldrich (Sigma Aldrich Ltd., USA). N,N-dimethyl formamide (DMF) with a purity of 99.9%, zinc acetate dihydrate ($Zn(CH_3COO)_2{\cdot}2H_2O$, ZnAc) with a purity of 99.5%, and manganese acetate tetrahydrate ($Mn(CH_3COO)_2{\cdot}4H_2O$, MnAc) with a purity of 98% were purchased from Carlo Erba (Carlo Erba Ltd., Italy). Analytical grade methylene blue (MB) was procured from Acros Organic (Acros Organics, Belgium), and all the chemical agents were utilized without further purification. Nitrogen gas (N_2), which had a purity of 99.90%, was purchased from Linde (Thailand) PCL., (Samutprakarn, Thailand).

2.2. Fabrication of Mn-doped ZnO composited carbon nanofibers (Mn-ZnO/CNFs)

Mn-doped ZnO/carbon nanofibers (Mn-ZnO/CNFs) were fabricated using manganese acetate (MnAc) as a dopant. First, 10 %w/v PAN in DMF was prepared and stirred to achieve a homogeneous solution suitable for fiber spinning. Then, 1.0 g of ZnAc was added into the PAN solution. Next, MnAc was dissolved into a solution of ZnAc/PAN at varying concentrations of 0, 1, 5, 10, 15, and 20 wt% relative to ZnAc. The resulting homogeneous solution was electrospun into nanofibers. The nanofibers were stabilized in air at 250 ℃ and held at this temperature for 2 h, followed by subsequent carbonation beneath a nitrogen atmosphere at 650 ℃ for 1 h. The obtained Mn-doped ZnO/CNFs were labeled as (1)Mn-ZnO/CNFs, (5)Mn-ZnO/CNFs, (10)Mn-ZnO/CNFs, (15)Mn-ZnO/CNFs, and (20)Mn-ZnO/CNFs, which corresponded to the respective MnAc precursor concentrations used.

2.3. Characterization

The surface morphology and elemental composition of the samples were observed using a Field Emission Scanning Electron Microscope equipped with an Energy Dispersive X-ray Spectrometer (FESEM-EDS, JSM-7610F, Oxford X-Max 20, JEOL, Japan). The fiber diameter size was measured using the SemAfore 5.21 image analyzer software (Insinooritoimisto J. Rimppi Oy, Finland). The

crystal structure of the samples was studied using an X-ray Diffractometer (XRD, AXS Model D8-Discover, Bruker, Germany) with Cu KD radiation at an accelerating voltage of 40 kV and emission current of 40 mA, in the 2θ angle range of 10° to 80°. The specific surface area and pore size distribution of the nanofibers were analyzed using a 3Flex Physisorption Surface Analyzer (Micromeritics Instrument, USA) and calculated by the Brunauer-Emmett-Teller (BET) and the Barret-Joyner-Halenda (BJH) methods. The surface chemical composition of the samples was studied using X-ray Photoelectron Spectroscopy (XPS, Model Axis ultra DLD, Kratos) equipped with an Al KD (1486.6 eV). The binding energy values were calibrated using the C (1s) line at 284.4 eV. The optical properties of the samples were determined using a UV-Visible Near-Infrared Spectrometer (Perkin Elmer, Lambda 950, USA).

2.4. Photocatalytic study

The photocatalytic degradation of the MB dye was conducted in a batch reactor using a catalyst membrane. The reactor setup consisted of utilizing a cylindrical glass vessel (7.5 cm inside diameter, 16.5 cm depth) equipped with a 7W ultraviolet C (UVC) lamp, as illustrated in Figure 1.

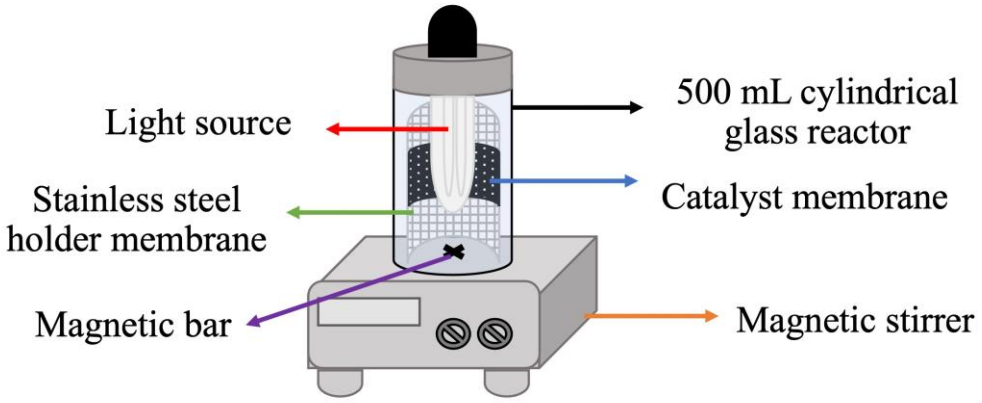

Figure 1. An image of the photo-reactor used for the photocatalytic degradation of MB.

A stainless-steel mesh sample holder was used to hold 50 mg of the catalyst membrane, which was fully immersed in 450 mL of an aqueous MB solution with a concentration of 10 mg/L. The solution was continuously stirred in darkness for 15 h to achieve an adsorption-desorption equilibrium. After establishing the MB adsorption equilibrium, the light was turned on, and the MB concentration at equilibrium was considered as the initial concentration for the photocatalytic reaction. For the photocatalysis under visible light, a 7W light-emitting diode (LED, Philips) was used as the visible light source, where the testing conditions were consistently maintained with those under UV light irradiation. At predetermined intervals, 2 mL of the solution with a decreased MB concentration were extracted and analyzed using a UV-vis spectrophotometer (T60, PG Instrument, UK) at a maximum wavelength of 664 nm. The MB removal efficiency was calculated using Eq 1:

$$D = [(C_0 - C_t) / C_0] \times 100 \quad (1)$$

Where C_0 is the MB dye concentration after adsorption, and C_t is the MB dye at time t.

3. Results and discussions

3.1. Morphology analysis of Mn-doped ZnO composited carbon nanofibers

Mn-doped ZnO/CNFs were synthesized by incorporating various weight percentages (1%, 5%, 10%, 15%, and 20% relative to ZnAc precursor) of the MnAc dopant into a ZnAc/PAN solution. The morphology of the obtained fibers was examined using FESEM after carbonization at 650°C, as shown in Figure 2. The analysis revealed that the fiber size of carbonized Mn-doped ZnO/CNFs increased with the escalating content of Mn dopant, ranging from 1145.4 ± 184 to 1491 ± 247 nm. Additionally, the surface morphology of the Mn-doped ZnO/CNFs appeared coarse and dense. This was attributed to the growth of Mn-doped ZnO particles, which were observed to emerge on the surface of the CNFs' skeleton. This phenomenon can be explained by the Kirkendall effect, where the diffusion asymmetry of atoms leads to the outward migration of ZnO species, consequently forming the coarse morphology observed on the CNFs surface [27].

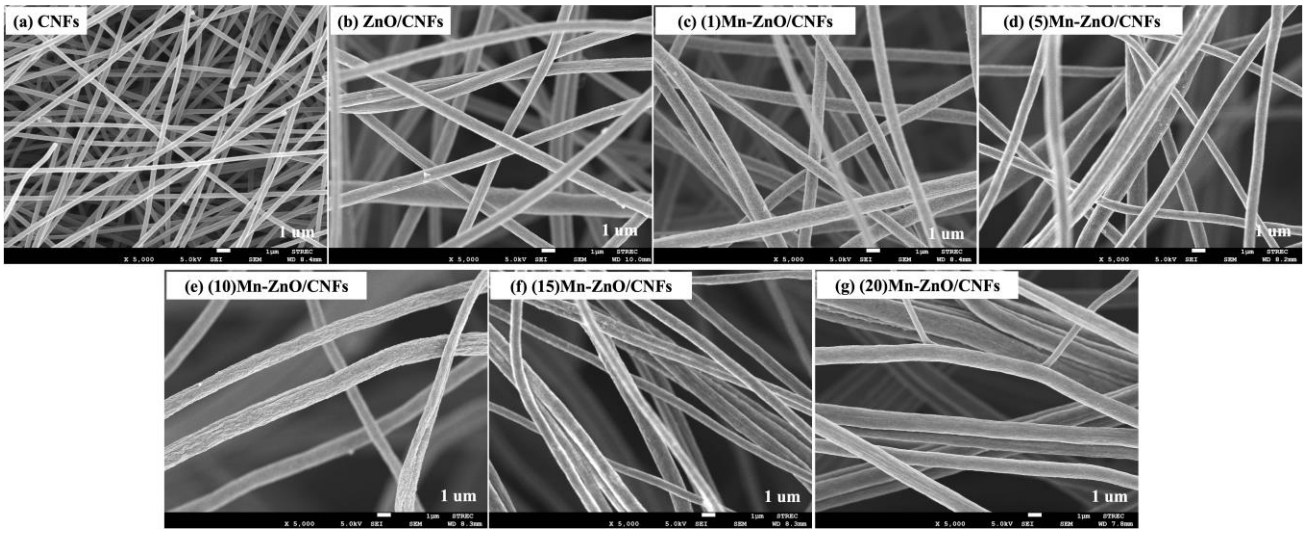

Figure 2. SEM images of (a) CNFs, (b) ZnO/CNFs, (c) (1)Mn-ZnO/CNFs, (d) (5)Mn-ZnO/CNFs, (e) (10)Mn-ZnO/CNFs, (f) (15)Mn-ZnO/CNFs, and (g) (20)Mn-ZnO/CNFs carbonization at 650°C.

Figure 3 shows the EDX spectrum and elemental mapping images of (1)Mn-ZnO/CNFs and (20)Mn-ZnO/CNFs after carbonization at 650°C. These samples exhibit the presence of high intensities of Zn atoms and low intensities of Mn atoms. Additionally, the high intensities of C and O can be seen. These atoms were distributed throughout the nanofibrous structure. Furthermore, the intensity of the Mn signal increased proportionally with the increment in the Mn dopant.

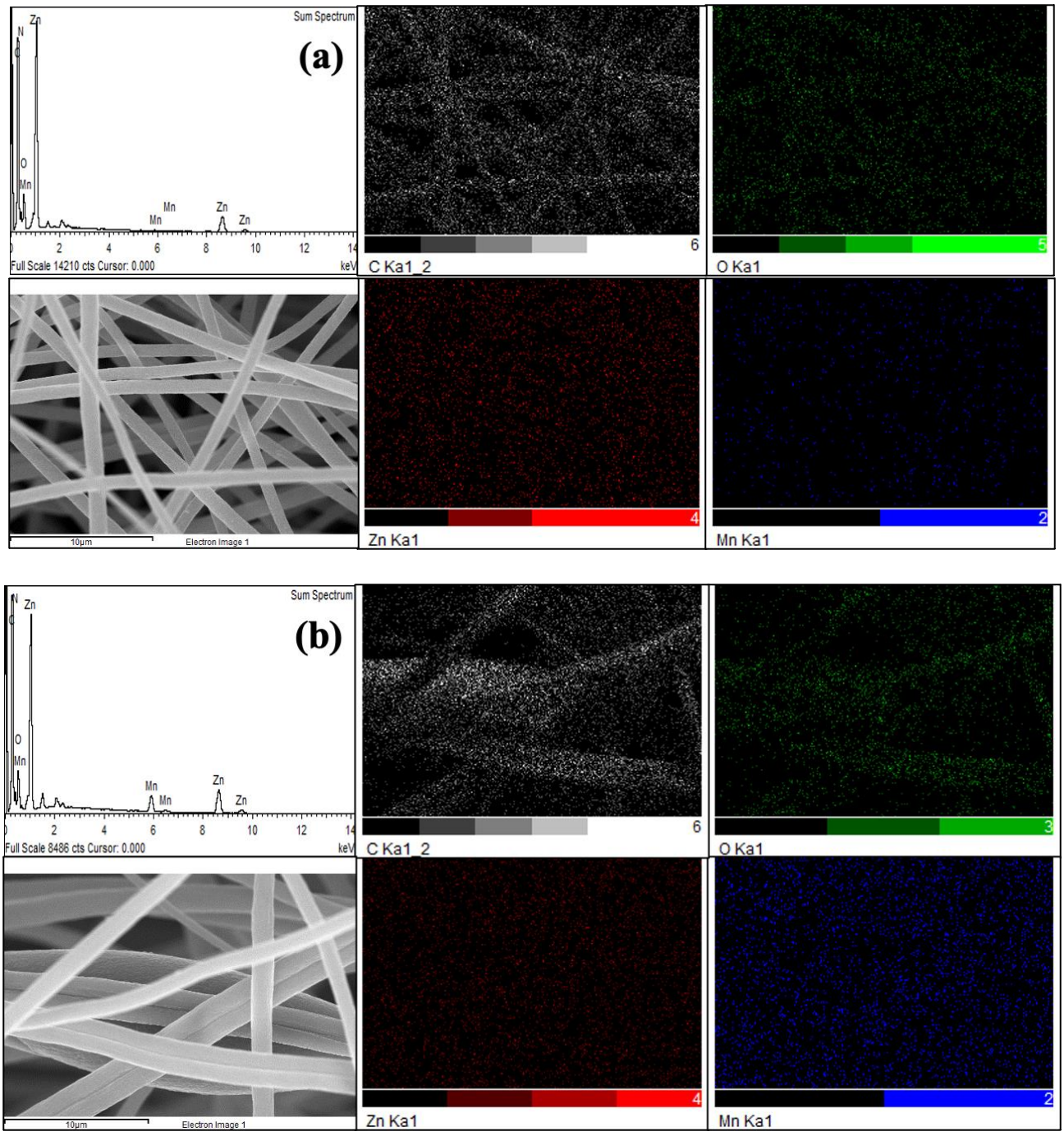

Figure 3. EDX spectrum and elemental mapping images of (a) (1)Mn-ZnO/CNFs, and (b) (20)Mn-ZnO/CNFs carbonized at 650°C.

Table 1 presents the calculated solid fraction and dopant mole fraction of a series of samples carbonized at 650°C. These calculations were based on the assumption of a homogeneous distribution of the polymer, semiconductor, and dopant precursor throughout the solution. It was assumed that there were no changes in the chemical reactions during the conversion process, and that a complete conversion of the samples was achieved after carbonization at 650°C. The solid fraction of pure CNFs was found to be 1.000. However, for the Mn-ZnO/CNFs samples, the solid fraction of both CNFs and ZnO showed a slight reduction, while the Mn solid fraction gradually increased with a rising amount

of Mn dopant. These findings suggest that the addition of the Mn dopant may have influenced the solid fraction of the resultant composite material.

The solid fraction and metal mole fraction were altered as the concentration of the Mn dopant increase (Table 1). For instance, the (1) Mn-ZnO/CNFs sample exhibited a slight reduction in the solid fraction compared to pure ZnO/CNFs, but with a small contribution of Mn. As the Mn dopant percentage increased in the (5), (10), (15), and (20) Mn-ZnO/CNFs samples, the solid fraction of both ZnO and CNFs decreased, while the Mn solid fraction correspondingly increased. These observations suggest that the incorporation of the Mn dopant into the ZnO/CNFs system influenced the material's overall composition, leading to changes in the solid fractions of the individual components.

Table 1. Expected solid fraction and dopant mole fraction of the samples after carbonization at 650°C (*Calculated from actual weight of metal acetate precursor).

Sample	Solid fraction			Metal mole fraction*	
	CNFs	ZnO	Mn	Zn	Mn
Pure CNFs	1.000	-	-	-	-
ZnO/CNFs	0.648	0.352	-	-	-
(1) Mn-ZnO/CNFs	0.647	0.351	0.002	0.990	0.010
(5) Mn-ZnO/CNFs	0.641	0.348	0.011	0.957	0.043
(10) Mn-ZnO/CNFs	0.634	0.345	0.021	0.918	0.082
(15) Mn-ZnO/CNFs	0.628	0.341	0.031	0.881	0.119
(20) Mn-ZnO/CNFs	0.621	0.338	0.041	0.848	0.152

3.2. XRD analysis of Mn-ZnO/CNFs

Figure 4a shows the crystal structure analysis of the CNFs, the ZnO/CNFs, and the Mn-doped ZnO/CNFs. The XRD pattern of the CNFs shows distinct peaks at 25.29º, which corresponds to the (002) plane of carbon structure in the CNFs. Compared with the pure CNFs, the composited nanofibers showed additional various peaks at 31.77°, 34.48°, 36.32°, 47.66°, 56.63°, 62.83°, 67.92°, 69.25°, which correspond to the (100), (002), (101), (102), (110), (103), (112), and (201) planes of the ZnO and Mn-doped ZnO/CNFs, confirming its hexagonal wurtzite crystal structure [28]. Notably, no impurity peaks were detected, indicating the successful incorporation of Mn^{2+} ions by substituting for Zn^{2+} ions in the ZnO lattice, rather than occupying the interstitial sites. The (100), (002), and (101) peaks of the Mn-doped ZnO/CNFs displayed a shift in the position of diffraction peaks with increasing Mn dopant concentration, as shown in Figure 4b. This shift is attributed to the 0.80 Å ionic radius of the Mn^{2+} ions, which is larger than that of the Zn^{2+} ions (0.74 Å) [29]. The crystallite size of the ZnO/CNFs and the Mn-doped ZnO/CNFs was calculated using the Scherrer's equation: $D = K\lambda / \beta \cos\theta$, where λ is the X-ray wavelength for CuKα radiation (λ = 1.5406 Å), K is the Scherrer constant taken as 0.9, β is the full width at half maximum (FWHM) in degrees, and θ is the Bragg angle of (100) and (101) peaks. The crystallite size of the ZnO/CNFs and a series of Mn-doped ZnO/CNFs (from 1 – 20 wt%) were found to be 7.13, 7.61, 8.23, 8.29, 7.11, and 7.96 nm, respectively, showing an increase in the crystallite size with an increasing Mn dopant concentration from 1% to 10%. Then the crystallite size decreased as Mn dopant concentration increased from 15% to 20%. This result was similar to the study by N. A. Putri et al., the crystallite size increased with increasing Mn dopant, while some studies demonstrate that the crystallite size decreases by Mn doping due to the ionic radius of Zn^{2+} smaller

than that of Mn^{2+} [30]. These results offer valuable insights into the crystal structure and composition of the Mn-doped ZnO/CNFs. Furthermore, the formation of an ordered graphite structure with an increasing Mn dopant suggests the coexistence of CNFs alongside the Mn-doped ZnO.

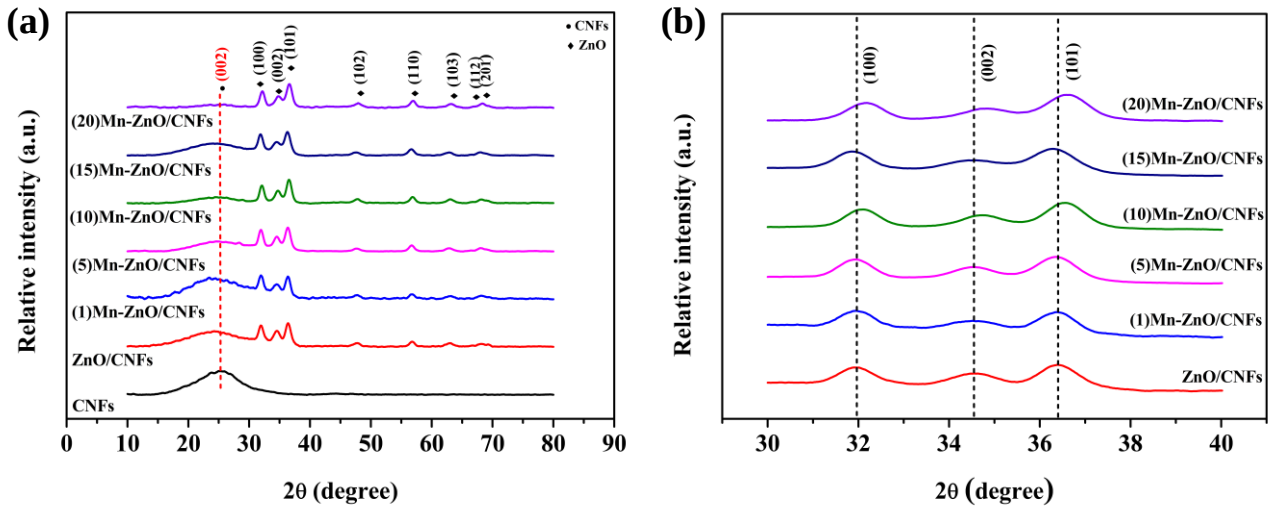

Figure 4. (a) XRD patterns of CNFs, ZnO/CNFs, and Mn-ZnO/CNFs carbonized at 650 ℃ under N_2 atmosphere, and (b) shifting of the XRD peaks from 30° to 40°.

3.3. XPS analysis of Mn-ZnO/CNFs

The XPS analysis was conducted to investigate the chemical composition and bonding state of the Mn-ZnO/CNFs material (Figure 5). The wide scan XPS spectrum showed the presence of C, N, O, Zn, and Mn in the sample (Figure 5a). In the high-resolution Zn 2p spectrum (Figure 5b), two distinct peaks at 1021.5 eV and 1044.5 eV were observed, which corresponded to Zn $2p_{3/2}$ and Zn $2p_{1/2}$, respectively, with a spin orbital-splitting of 23.0 eV. This indicates the presence of Zn^{2+} ions in the ZnO wurtzite structure [28,31]. The Mn 2p spectrum (Figure 5c) showed two peaks at 641.2 and 655 eV, attributed to Mn $2p_{3/2}$ and Mn $2p_{1/2}$, respectively, which confirmed the presence of Mn^{2+} ions in the Mn-ZnO/CNFs [28]. The O 1s spectrum (Figure 5d) displayed two peaks at 531.1 and 533.5 eV., which determined O^{2-} ions in the Zn-O bond and the oxygen-deficient regions, respectively [24,31]. The C 1s spectrum (Figure 5e) revealed four peaks at 284.8, 286.2, 286.9, and 288.2 eV, which corresponded to C-C bonds in either the CNFs structure or adventitious carbon, C-C or C-O bonds, Zn-O-C bonds, and C=O bonds, respectively [32,33]. Notably, there was no evidence of zinc carbide (Zn-C) formation, which indicated that C atoms did not substitute O in the crystal structure of Mn-ZnO/CNFs [34,35]. The N 1s spectrum (Figure 5f) exhibited two components at 398.4 and 399.4 eV, which were assigned to pyridinic N and either pyrrolic N or graphitic, respectively [31,36].

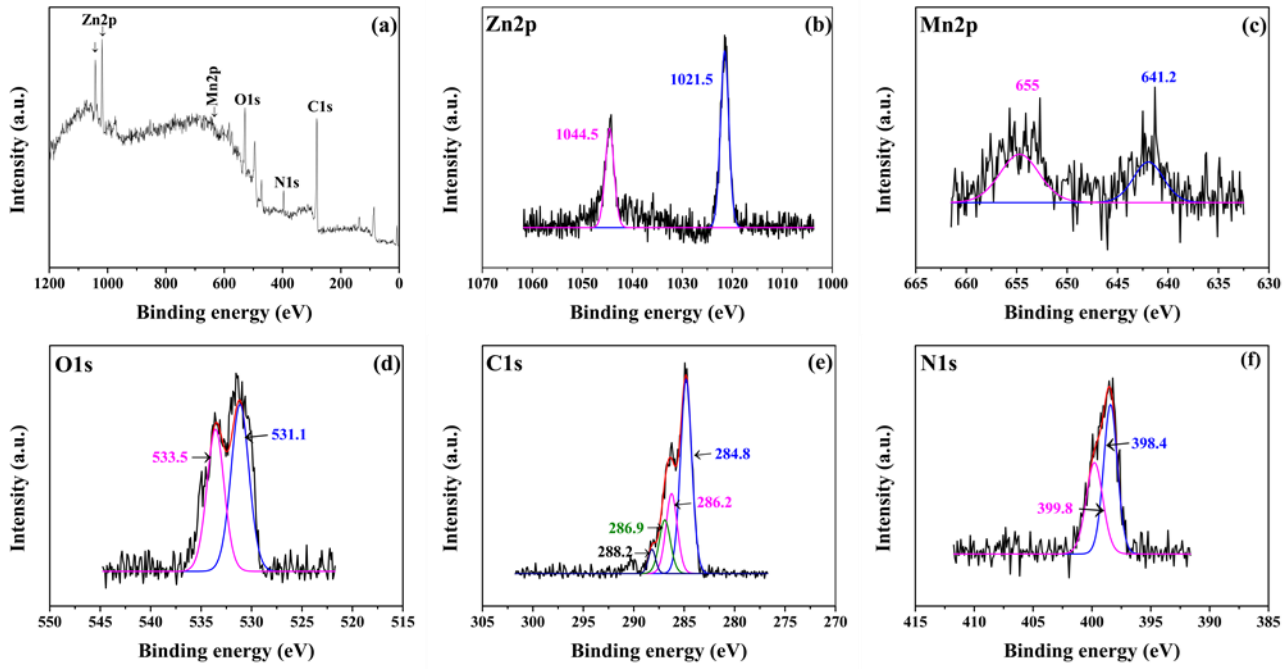

Figure 5. The XPS spectra of (a) wide scan of (20)Mn-ZnO/CNFs, (b) Zn2p core level of (20)Mn-ZnO/CNFs, (c) Mn2p core level of (20)Mn-ZnO/CNFs, and (d-f) O1s, C1s, and N1s core level of (20)Mn-ZnO/CNFs.

3.4. Specific surface area analysis of Mn-ZnO/CNF

Surface area, defects, and surface hydroxyl groups have been generally recognized for the enhancement of photocatalytic efficiency [37]. N_2 adsorption-desorption isotherms were used to investigate a series of Mn-ZnO/CNFs with varying Mn dopant concentrations, focusing on the impact of the fibrous structure and porosity (Figure 6a). The results revealed a type IV isotherm with a hysteresis loop in the middle of a high relative pressure region. This is due to the introduction of Mn-ZnO nanoparticles, which induced a mesoporous structure within the fibrous network of the CNFs. The specific surface area of the Mn-ZnO/CNFs was found to be dependent on the concentration of the Mn-ZnO nanoparticles. The specific surface area ranged from 4.33 to 17.24 m^2/g, indicating a significant variation with a varying Mn dopant content. Furthermore, the pore size distribution of the Mn-ZnO/CNFs was also investigated (Figure 6b). The analysis data demonstrated that the incorporation of both zinc acetate and the Mn dopant played a crucial role in augmenting the surface area and pore structure of the CNFs. This observation suggests that the elimination of organic moieties and the volatilization of compounds such as CO, CO_2, H_2, and CH_4, along with the formation of ZnO through the release of acetate from the zinc acetate. The collective contribution to the creation of a porous structure and the consequent increased the specific surface area [32]. As indicated by the XRD result, there is a discernible change in the crystallite size of the samples with Mn doping fraction. This change in the crystallite size, along with Mn-ZnO distribution in CNFs, could contribute to change in specific surface area and a concurrent decrease in the pore size founded in this study. In general, these alterations were anticipated to be advantageous for augmenting both the adsorption performance and the photocatalytic activity of the materials [29,38].

Table 2. Surface properties of pure CNFs, ZnO/CNFs and Mn-ZnO/CNFs.

Sample	Specific surface area (m^2/g)	Average pore size (Å)	Total pore volume (cm^2/g)
CNF	9.31	288.26	0.009
ZnO/CNFs	12.69	231.82	0.054
(1) Mn-ZnO/CNFs	17.24	200.74	0.063
(5) Mn-ZnO/CNFs	11.34	255.95	0.059
(10) Mn-ZnO/CNFs	4.33	363.56	0.013
(15) Mn-ZnO/CNFs	9.98	126.81	0.027
(20) Mn-ZnO/CNFs	16.81	193.39	0.037

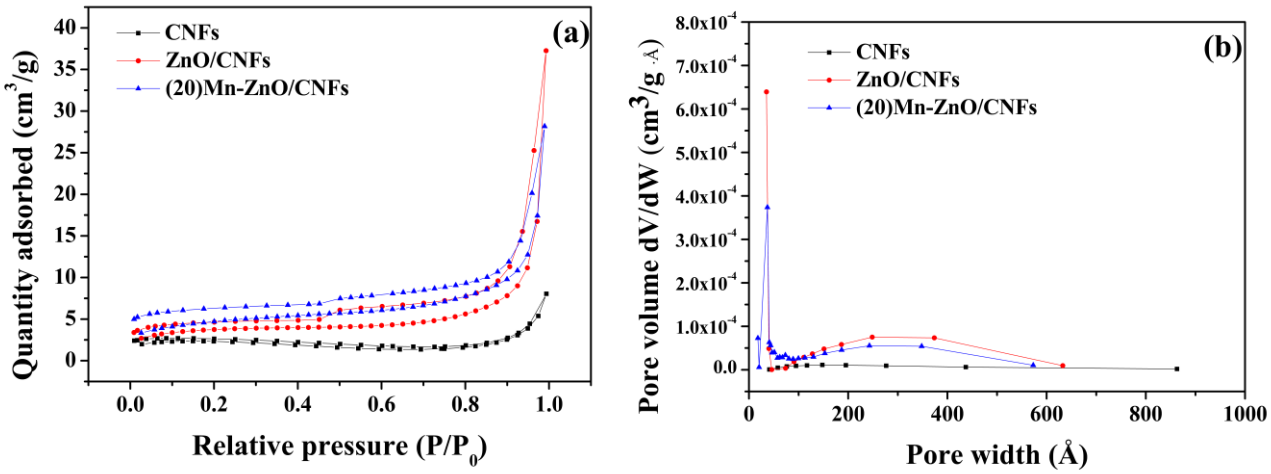

Figure 6. (a) N_2 adsorption-desorption isotherm, and (b) Barrett-Joyner-Halenda (BJH) pore size distribution curve of CNFs, ZnO/CNFs and (20)Mn-ZnO/CNFs carbonized at 650 ℃.

3.5. Optical properties of Mn-ZnO/CNF

The optical band gap properties of the Mn-ZnO/CNFs are presented in Figure 7. The UV-Vis absorption spectra of the Mn-ZnO/CNFs samples were shown in Figure 7a. The photo-response of the samples in the UV and visible regions was observed due to the presence of oxygen vacancies as expected from XPS results was observed. The energy gap of the samples was calculated using Tauc's equation (Eq 2), which is commonly used to determine the band gap of semiconducting materials. The equation is shown below:

$$(\alpha h\upsilon)^2 = A\,(h\upsilon - E_g) \tag{2}$$

Where α is the adsorption coefficient of the material, A is a proportionality constant, h is the Planck's constant, υ is the frequency of light, and E_g is the band gap energy. The band gap was estimated by plotting a function of $(\alpha h\upsilon)^2$ vs. photon energy (hυ) and extrapolating the linear part of the graph to the x-axis, which will give the value of the band gap.

The band gap energy of the ZnO/CNFs and different Mn-doped ZnO/CNFs samples, labeled as (1)Mn-ZnO/CNFs, (5)Mn-ZnO/CNFs, (10)Mn-ZnO/CNFs, (15)Mn-ZnO/CNFs, and (20)Mn-ZnO/CNFs, were determined as follows: ZnO/CNFs had a band gap energy of 2.95 eV, (1)Mn-ZnO/CNFs had 2.79 eV, (5)Mn-ZnO/CNFs had 2.76 eV, (10)Mn-ZnO/CNFs had 2.86 eV, (15)Mn-ZnO/CNFs had 2.88 eV, and (20)Mn-ZnO/CNFs had 2.91 eV. Comparing these values to the bulk ZnO, which typically has a band gap energy of approximately 3.37 eV, it was obvious that the ZnO/CNFs and Mn-ZnO/CNFs exhibited lower band gap energies. The band gap energy of Mn-ZnO/CNFs could be modified and tuned to some degree with change in Mn doping concentration. We anticipate that further optimization in other processing parameters such as carbonization/calcification temperature, would enhance the tunability of electronic properties of materials even further and would be beneficial for photocatalytic application.

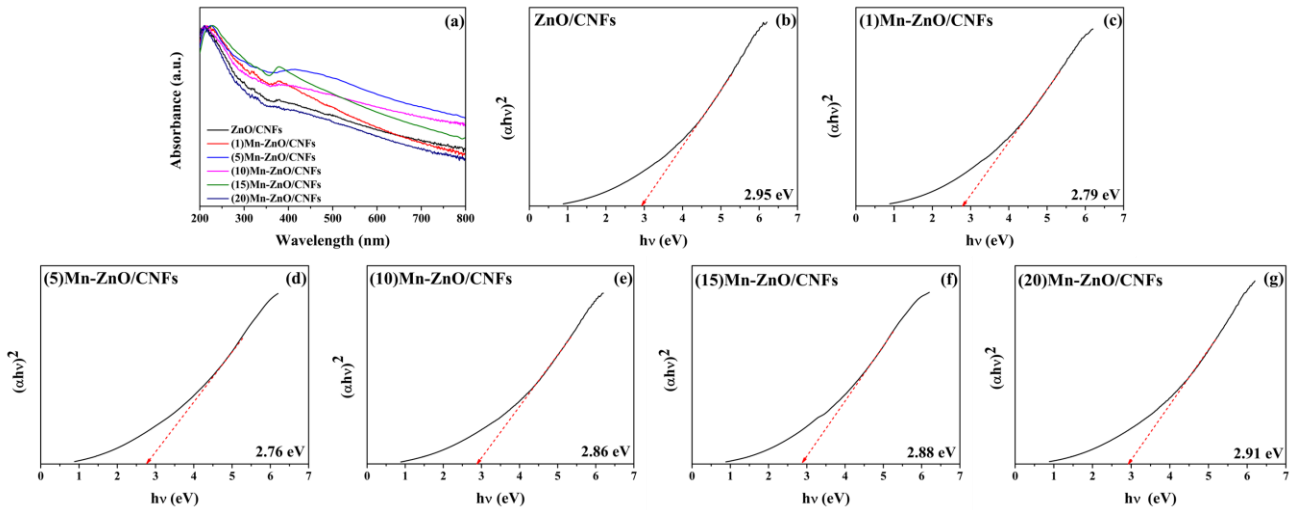

Figure 7. (a) UV-visible spectra of ZnO/CNFs and Mn-ZnO/CNFs with different Mn content. And Tauc plots for (b) ZnO/CNFs, (c) (1)Mn-ZnO/CNFs, (d) (5)Mn-ZnO/CNFs, (e) (10)Mn-ZnO/CNFs, (f) (15)Mn-ZnO/CNFs, and (g) (20)Mn-ZnO/CNFs carbonized at 650 °C under N_2 atmosphere**.**

3.6. Photocatalytic activity

The photocatalytic activity of undoped and Mn-doped ZnO/CNFs samples was investigated for the degradation of MB in an aqueous solution under UV light irradiation, as depicted in Figure 8. In the absence of a catalyst membrane, MB degradation proceeded, reaching approximately 65% degradation within the experimental time frame. However, the introduction of catalyst membranes significantly improved the degradation efficiency. The addition of ZnO/CNFs, (1) Mn-ZnO/CNFs, (5) Mn-ZnO/CNFs, (10) Mn-ZnO/CNFs, (15) Mn-ZnO/CNFs, and (20) Mn-ZnO/CNFs catalyst membranes resulted in degradation efficiencies of approximately 81%, 83%, 91%, 87%, 85%, and 82%, respectively. These findings indicate that the catalyst membranes enhanced the degradation of MB, and the efficiency varied with different Mn dopant contents. Notably, the highest photocatalytic degradation performance was observed in the (5) Mn-ZnO/CNFs sample, which contained a 5 wt% Mn dopant. This result aligns with the band gap energy calculation, which showed the lowest value of

approximately 2.76 eV for this sample. The enhanced photocatalytic activity with a 5 wt% Mn dopant can be attributed to the modified electronic structure and reduced band gap energy, thus promoting an efficient charge separation and enhancing photo-generated electron-hole pairs. The introduction of Mn dopants in this concentration range seems to offer the most favorable conditions for effective photocatalysis. These results underscore the importance of Mn doping to optimize the photocatalytic performance of the ZnO/CNFs and suggest that careful control of the Mn dopant content can lead to enhanced degradation efficiency for MB and potentially other organic pollutants. The photocatalytic behavior demonstrated in this study holds promise for applications in wastewater treatment and environmental remediation. Further research could explore the underlying mechanisms behind the optimized photocatalytic behavior of the (5) Mn-ZnO/CNFs sample and its potential for broader practical applications.

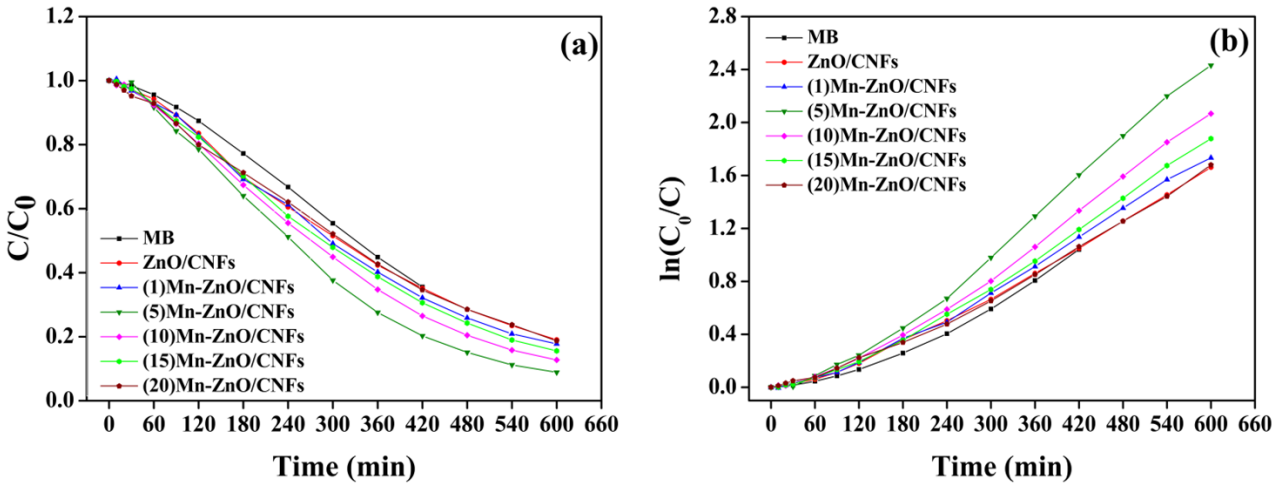

Figure 8. Comparison of photocatalytic degradation of MB dye under UV light irradiation at different numbers of Mn-doped ZnO/CNFs carbonized at 650 ℃.

To further investigate the kinetic reaction rate of the photocatalyst membranes, the Langmuir-Hinshelwood (L-H) model was employed. When the MB concentration was dilute, the kinetic rate could be assumed as a pseudo-first-order reaction, which can be described by Eq 3:

$$\ln(C_0/C) = kt \quad (3)$$

Where C_0 is the initial concentration of MB (mg/L), C is the residual concentration of MB at time *t* (min), and k is the reaction rate constant (min^{-1}). The calculation of the kinetic rate is summarized in Table 3.

Table 3. Effect of Mn doping concentration on the kinetic rate reaction and degradation rate of the photocatalyst membranes on photocatalytic degradation of MB dye under UV light irradiation.

Sample	K (min^{-1})	R^2	D (%)
ZnO/CNFs	0.0026	0.989	81.0 ± 1.7
(1) Mn-ZnO/CNFs	0.0027	0.988	82.5 ± 2.1
(5) Mn-ZnO/CNFs	0.0038	0.985	91.2 ± 1.4
(10) Mn-ZnO/CNFs	0.0032	0.986	87.4 ± 1.8
(15) Mn-ZnO/CNFs	0.0029	0.986	84.6 ± 3.3
(20) Mn-ZnO/CNFs	0.0026	0.989	81.6 ± 1.6

The results obtained in this study were in good agreement with the L-H (Langmuir-Hinshelwood) model, as evidenced by high R^2 values exceeding 0.98 in all cases. The kinetic rate constants for the Mn-ZnO/CNFs photocatalysts ranged from 0.0026 to 0.0038 min^{-1}, depending on the Mn dopant concentration, with the highest value observed for the (5) Mn-ZnO/CNFs sample. These findings indicate that increasing the precursor loading content can enhance the photocatalytic activity of the photocatalyst membranes. The observed enhancement in the photocatalytic activity can be attributed to several factors. First, the increase in the precursor loading content led to higher specific surface areas in the Mn-ZnO/CNFs, as discussed in section 3.4, providing more active sites for MB adsorption and degradation. Additionally, the efficient electron-hole pair separation facilitated by the Mn dopant enhanced the overall photocatalytic efficiency. This improved electron-hole pair separation reduced the chances of charge recombination and boosted the photocatalytic degradation process. The combination of enhanced adsorption due to a higher specific surface area and an improved degradation efficiency from the efficient charge separation results in an overall increase in photocatalytic activity for the (5) Mn-ZnO/CNFs sample. These findings align with previous studies [24,25] that have demonstrated the importance of a specific surface area and charge separation in influencing the photocatalytic performance.

The photocatalytic degradation of the MB dye was investigated using a 7W LED lamp as the visible light source, employing an experimental setup similar to the one used for photocatalysis under UV light irradiation. The results, presented in Figure 9, indicated a slight decrease in the degradation rate of the MB dye under visible light irradiation without the photocatalyst membrane. This suggests that the MB dye could undergo decomposition under visible light, though the degradation process might be slower compared to UV light. In contrast, the presence of photocatalyst membranes demonstrated an efficient performance under visible light irradiation. The kinetic rate constants, summarized in Table 4, ranged from approximately 0.0001 to 0.0004 min^{-1} for the different Mn-ZnO/CNFs photocatalysts. This indicates that the photocatalyst membranes can effectively degrade the MB dye even in the presence of visible light. However, the photocatalytic efficiency observed under visible light irradiation was lower compared to that under UV light irradiation. This discrepancy suggests that UV light provides an optimal number of photons, which are essential to achieve an effective photocatalytic degradation of the MB dye. The results of this study align with previous research [39] that has shown the importance of the light source in determining the photocatalytic efficiency of the photocatalyst. With its higher energy photons, UV light appears to be more suitable for promoting the photocatalytic degradation process compared to visible light, which has lower energy photons.

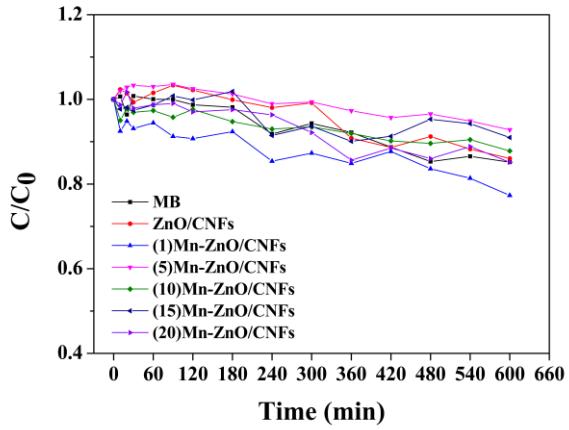

Figure 9. Comparison of photocatalytic degradation of MB dye under visible light irradiation at different numbers of Mn-doped ZnO/CNFs carbonized at 650 ℃.

Table 4. Effect of Mn doping concentration on the kinetic rate reaction and degradation rate of the photocatalyst membranes on photocatalytic degradation of MB dye under visible light irradiation.

Sample	K (min^{-1})	R^2	D (%)
ZnO/CNFs	0.0002	0.819	14.0 ± 3.8
(1) Mn-ZnO/CNFs	0.0004	0.912	22.7 ± 7.4
(5) Mn-ZnO/CNFs	0.0001	0.514	7.2 ± 3.6
(10) Mn-ZnO/CNFs	0.0002	0.934	12.2 ± 2.8
(15) Mn-ZnO/CNFs	0.0002	0.784	9.0 ± 9.3
(20) Mn-ZnO/CNFs	0.0003	0.938	14.9 ± 0.6

It is well known that the photocatalytic efficiency of semiconductors is governed by the surface area, surface defect, surface hydroxyl groups, structure of materials, and photoabsorption [37,40]. In this study, Mn-doped ZnO composite CNFs exhibited higher specific surface and mesopores, as seen in Table 2, as well as an oxygen defect in ZnO, which is shown in Figure 5. The incorporation of CNFs in the synthesis of photocatalysts has been shown to significantly enhance their photocatalytic activity. This improvement can be attributed to several key factors. First, CNFs possess excellent light absorption properties, enabling them to efficiently capture light irradiation. Subsequently, the photogenerated electrons are effectively transferred to either the conduction band of ZnO or to the energy level of Mn^{2+} within ZnO, promoting efficient electron-hole separation. This enhanced charge separation is crucial to achieve a higher photocatalytic activity [34,37,41]. The photogenerated electrons, present in the conduction band of ZnO or Mn-doped ZnO, participate in reactions with adsorbed O_2, leading to the formation of superoxide anion radicals ($•O_2^-$). Simultaneously, the holes react with H_2O molecules to generate highly reactive hydroxyl radicals (•OH) and hydrogen peroxide (H_2O_2). These reactive species, $•O_2^-$, •OH, and H_2O_2, serve as potent oxidizing agents, initiating a series of oxidative reactions that facilitate the degradation of the MB dye molecules into harmless byproducts, such as CO_2 and H_2O [24,40,42,43]. By harnessing the synergistic effects of the CNFs and Mn-doped ZnO, the photocatalyst membranes exhibit an improved efficiency in the degradation of the MB dye. The enhanced photocatalytic activity and efficient generation of reactive species make these

materials promising candidates for applications in wastewater treatment and environmental remediation.

4. Conclusions

The study synthesized Mn-ZnO/CNFs and compared them to undoped ZnO/CNFs. SEM showed the Mn-ZnO/CNFs' rougher surface. The integration of Mn-doped ZnO onto the CNFs was confirmed by EDX, XRD, and XPS techniques. The catalyst used in the synthesis increased the specific surface area, and a N_2 adsorption-desorption isotherm indicated a mesoporous structure. The photocatalytic activity was evaluated using an MB dye, with the Mn-Zn/CNFs showing high degradation rates between 81% and 91%. The kinetics of the reaction were described using the simplified Langmuir-Hinshelwood equation, which enhanced the understanding of the material's properties and highlighted the potential for environmental remediation. Future investigations are recommended to comprehensively compare these Mn-ZnO/CNFs with those produced by alternative methods, such as hydrothermal or dip coating, to evaluate their properties and photocatalytic activity. Additionally, testing the Mn-ZnO/CNFs under more intense visible light irradiation could reveal their performance under natural sunlight-like conditions, expanding their practical applications.

Use of AI tools declaration

The authors declare they have not used Artificial Intelligence (AI) tools in the creation of this article.

Acknowledgments

All authors participated in the conceptualization, methodology, and software development of this study, with Krittiya Singcharoen taking the lead in conducting the primary experiment and performing the characterization. Krittiya Singcharoen was also responsible for drafting the initial manuscript. Ratthapol Rangkupan, Thanakorn Wasanapiarnpong, and Soontree Khuntong provided critical feedback during the review, editing, and data visualization stages. Thanakorn Wasanapiarnpong oversaw the supervision, and project administration. Ratthapol Rangkupan oversaw the supervision, project administration, and funding acquisition. The final version of the manuscript has undergone thorough review and approval for publication by all authors.

The present research was made possible through funding provided by the "The 100th Anniversary Chulalongkorn University Fund for Doctoral Scholarship", "The 90th Anniversary of Chulalongkorn University Fund (Ratchadaphiseksomphot Endowment Fund)", and "Ratchadapiseksomphot Grant, Chulalongkorn University (CU-GR-63-53-62-03)".

Conflict of Interest

The authors declare no conflict of interest.

References

1. Al-Tohamy R, Ali SS, Li F, et al. (2022) A critical review on the treatment of dye-containing wastewater: Ecotoxicological and health concerns of textile dyes and possible remediation approaches for environmental safety. *Ecotoxicol Environ Saf* 231: 113160. https://doi.org/10.1016/j.ecoenv.2021.113160
2. Piaskowski K, Świderska-Dąbrowska R, Zarzycki PK (2018) Dye Removal from Water and Wastewater Using Various Physical, Chemical, and Biological Processes. *J AOAC Int* 101: 1371–1384. https://doi.org/10.5740/jaoacint.18-0051
3. Peramune D, Manatunga DC, Dassanayake RS, et al. (2022) Recent advances in biopolymer-based advanced oxidation processes for dye removal applications: A review. *Environ Res* 215: 114242. https://doi.org/10.1016/j.envres.2022.114242
4. Buzzetti L, Crisenza GEM, Melchiorre P (2019) Mechanistic Studies in Photocatalysis. *Angewandte Chemie Int Ed* 58: 3730–3747. https://doi.org/10.1002/anie.201809984
5. Ângelo J, Andrade L, Madeira LM, et al. (2013) An overview of photocatalysis phenomena applied to NOx abatement. *J Environ Manage* 129: 522–539. https://doi.org/10.1016/j.jenvman.2013.08.006
6. Sarkodie B, Amesimeku J, Frimpong C, et al. (2023) Photocatalytic degradation of dyes by novel electrospun nanofibers: A review. *Chemosphere* 313: 137654. https://doi.org/10.1016/j.chemosphere.2022.137654
7. Pomilla FR, García-López EI, Marcì G, et al. (2021) Heterogeneous photocatalytic materials for sustainable formation of high-value chemicals in green solvents. *Mater Today Sustain* 13: 100071. https://doi.org/10.1016/j.mtsust.2021.100071
8. Jadoun S, Yáñez J, Mansilla HD, et al. (2022) Conducting polymers/zinc oxide-based photocatalysts for environmental remediation: a review. *Environ Chem Lett* 20: 2063–2083. https://doi.org/10.1007/s10311-022-01398-w
9. Lee KM, Lai CW, Ngai KS, et al. (2016) Recent developments of zinc oxide based photocatalyst in water treatment technology: A review. *Water Res* 88: 428–448. https://doi.org/10.1016/j.watres.2015.09.045
10. Mohamed KM, Benitto JJ, Vijaya JJ, et al. (2023) Recent Advances in ZnO-Based Nanostructures for the Photocatalytic Degradation of Hazardous, Non-Biodegradable Medicines. *Crystals* 13. https://doi.org/10.3390/cryst13020329
11. Mao T, Liu M, Lin L, et al. (2022) A Study on Doping and Compound of Zinc Oxide Photocatalysts. *Polymers* 14. https://doi.org/10.3390/polym14214484
12. Ab Wahab N, Sairi NA, Alias Y (2022) Photocatalytic activities enhancement of manganese doped ZnO by decoration on CNT for degradation of organic pollutants under solar irradiation. *Appl Phys A Mater Sci Process* 128: 1–10. https://doi.org/10.1007/s00339-021-05160-x
13. Thakur P, Chahar D, Taneja S, et al. (2020) A review on MnZn ferrites: Synthesis, characterization and applications. *Ceram Int* 46: 15740–15763. https://doi.org/10.1016/j.ceramint.2020.03.287
14. Ullah R, Dutta J (2008) Photocatalytic degradation of organic dyes with manganese-doped ZnO nanoparticles. *J Hazard Mater* 156: 194–200. https://doi.org/10.1016/j.jhazmat.2007.12.033
15. Ayoub I, Kumar V, Abolhassani R, et al. (2022) Advances in ZnO: Manipulation of defects for enhancing their technological potentials. *Nanotechnol Rev* 11: 575–619. https://doi.org/10.1515/ntrev-2022-0035

16. Rauf MA, Meetani MA, Hisaindee S (2011) An overview on the photocatalytic degradation of azo dyes in the presence of TiO2 doped with selective transition metals. *Desalination* 276: 13–27. https://doi.org/10.1016/j.desal.2011.03.071
17. Xu J-J, Lu Y-N, Tao F-F, et al. (2023) ZnO Nanoparticles Modified by Carbon Quantum Dots for the Photocatalytic Removal of Synthetic Pigment Pollutants. *ACS Omega* 8: 7845–7857. https://doi.org/10.1021/acsomega.2c07591
18. Chabalala MB, Al-Abri MZ, Mamba BB, et al. (2021) Mechanistic aspects for the enhanced adsorption of bromophenol blue and atrazine over cyclodextrin modified polyacrylonitrile nanofiber membranes. *Chem Eng Res Des* 169: 19–32. https://doi.org/10.1016/j.cherd.2021.02.010
19. Ferrone E, Araneo R, Notargiacomo A, et al. (2019) ZnO Nanostructures and Electrospun ZnO–Polymeric Hybrid Nanomaterials in Biomedical, Health, and Sustainability Applications. *Nanomaterials* 9. https://doi.org/10.3390/nano9101449
20. Asgari S, Mohammadi Ziarani G, Badiei A, et al. (2022) Electrospun composite nanofibers as novel high-performance and visible-light photocatalysts for removal of environmental pollutants: A review. *Environ Res* 215: 114296. https://doi.org/10.1016/j.envres.2022.114296
21. Li C, Yang J, Zhang L, et al. (2021) Carbon-based membrane materials and applications in water and wastewater treatment: a review. *Environ Chem Lett* 19: 1457–1475. https://doi.org/10.1007/s10311-020-01112-8
22. Wang W, Chen Y, Wang N, et al. (2022) Multifunction ZnO/carbon hybrid nanofiber mats for organic dyes treatment via photocatalysis with enhanced solar-driven evaporation. *Front Mater Sci* 16. https://doi.org/10.1007/s11706-022-0623-7
23. Wang Y, Hao X, Wang Z, et al. (2020) Facile fabrication of Mn2+- doped ZnO photocatalysts by electrospinning. *R Soc Open Sci* 7. https://doi.org/10.1098/rsos.191050
24. Baylan E, Altintas Yildirim O (2019) Highly efficient photocatalytic activity of stable manganese-doped zinc oxide (Mn:ZnO) nanofibers via electrospinning method. *Mater Sci Semicond Process* 103: 104621. https://doi.org/10.1016/j.mssp.2019.104621
25. Wang Y, Cheng J, Yu S, et al. (2016) Synergistic effect of N-decorated and Mn2+ doped ZnO nanofibers with enhanced photocatalytic activity. *Sci Rep* 6. https://doi.org/10.1038/srep32711
26. Samadi M, Zirak M, Naseri A, et al. (2016) Recent progress on doped ZnO nanostructures for visible-light photocatalysis. *Thin Solid Films* 605: 2–19. https://doi.org/10.1016/j.tsf.2015.12.064
27. Dai Z, Zhang CY, Guowen S, et al. (2020) Highly enhanced electrochemical cycling stabilities of hierarchical partially-embedded MnO/carbon nanofiber composites as supercapacitor electrodes. *Mat Sci Eng B* 262: 114684. https://doi.org/10.1016/j.mseb.2020.114684
28. Suganthi K, Vinoth E, Sudha L, et al. (2023) Manganese (Mn2+) doped hexagonal prismatic zinc oxide (ZnO) nanostructures for chemiresistive NO2 sensor. *Sens Actuators B Chem* 380: 133293. https://doi.org/10.1016/j.snb.2023.133293
29. Akram R, Fatima A, Almohaimeed ZM, et al. (2023) Photocatalytic Degradation of Methyl Green Dye Mediated by Pure and Mn-Doped Zinc Oxide Nanoparticles under Solar Light Irradiation. *Adsorpt Sci Technol* 2023. https://doi.org/10.1155/2023/5069872
30. Putri NA, Fauzia V, Iwan S, et al. (2018) Mn-doping-induced photocatalytic activity enhancement of ZnO nanorods prepared on glass substrates. *Appl Surf Sci* 439: 285–297. https://doi.org/10.1016/j.apsusc.2017.12.246

31. Samuel E, Joshi B, Kim M-W, et al. (2019) Hierarchical zeolitic imidazolate framework-derived manganese-doped zinc oxide decorated carbon nanofiber electrodes for high performance flexible supercapacitors. *Chem Eng J* 371: 657–665. https://doi.org/10.1016/j.cej.2019.04.065
32. Kim CH, Kim B-H (2015) Zinc oxide/activated carbon nanofiber composites for high-performance supercapacitor electrodes. *J Power Sources* 274: 512–520. https://doi.org/10.1016/j.jpowsour.2014.10.126
33. Luo Q, Yang X, Zhao X, et al. (2017) Facile preparation of well-dispersed ZnO/cyclized polyacrylonitrile nanocomposites with highly enhanced visible-light photocatalytic activity. *Appl Catal B* 204: 304–315. https://doi.org/10.1016/j.apcatb.2016.11.037
34. Samadi M, Shivaee HA, Zanetti M, et al. (2012) Visible light photocatalytic activity of novel MWCNT-doped ZnO electrospun nanofibers. *J Mol Catal A Chem* 359: 42–48. https://doi.org/10.1016/j.molcata.2012.03.019
35. Samadi M, Shivaee HA, Pourjavadi A, et al. (2013) Synergism of oxygen vacancy and carbonaceous species on enhanced photocatalytic activity of electrospun ZnO-carbon nanofibers: Charge carrier scavengers mechanism. *Appl Catal A Gen* 466: 153–160. https://doi.org/10.1016/j.apcata.2013.06.024
36. Ning H, Xie H, Zhao Q, et al. (2017) Electrospinning ZnO/carbon nanofiber as binder-free and self-supported anode for Li-ion batteries. *J Alloys Compd* 722: 716–720. https://doi.org/10.1016/j.jallcom.2017.06.099
37. Achouri F, Corbel S, Balan L, et al. (2016) Porous Mn-doped ZnO nanoparticles for enhanced solar and visible light photocatalysis. *Mater Des* 101: 309–316. https://doi.org/10.1016/j.matdes.2016.04.015
38. Liu L, Liu Z, Yang Y, et al. (2018) Photocatalytic properties of Fe-doped ZnO electrospun nanofibers. *Ceram Int* 44: 19998–20005. https://doi.org/10.1016/j.ceramint.2018.07.268
39. Alkaykh S, Mbarek A, Ali-Shattle EE (2020) Photocatalytic degradation of methylene blue dye in aqueous solution by MnTiO3 nanoparticles under sunlight irradiation. *Heliyon* 6: e03663. https://doi.org/10.1016/j.heliyon.2020.e03663
40. Wang D, Zhang M, Zhuang H, et al. (2017) The photocatalytic properties of hollow (GaN)1-x(ZnO)x composite nanofibers synthesized by electrospinning. *Appl Surf Sci* 396: 888–896. https://doi.org/10.1016/j.apsusc.2016.11.053
41. Xu Z, Li X, Wang W, et al. (2016) Microstructure and photocatalytic activity of electrospun carbon nanofibers decorated by TiO2 nanoparticles from hydrothermal reaction/blended spinning. *Ceram Int* 42: 15012–15022. https://doi.org/10.1016/j.ceramint.2016.06.150
42. Shah AP, Jain S, Mokale VJ, et al. (2019) High performance visible light photocatalysis of electrospun PAN/ZnO hybrid nanofibers. *J Ind Eng Chem* 77: 154–163. https://doi.org/10.1016/j.jiec.2019.04.03
43. Lakshmi K, Kadirvelu K, Mohan PS (2018) Photo-decontamination of p-nitrophenol using reusable lanthanum doped ZnO electrospun nanofiber catalyst. *J Mater Sci Mater El* 29: 12109–12117. https://doi.org/10.1007/s10854-018-9317-4